Check for updates

Analysis of External and Internal Disorder to Understand Band-Like Transport in n-Type Organic Semiconductors

Marc-Antoine Stoeckel, Yoann Olivier, Marco Gobbi, Dmytro Dudenko, Vincent Lemaur, Mohamed Zbiri, Anne A. Y. Guilbert, Gabriele D'Avino, Fabiola Liscio, Andrea Migliori, Luca Ortolani, Nicola Demitri, Xin Jin, Young-Gyun Jeong, Andrea Liscio, Marco-Vittorio Nardi, Luca Pasquali, Luca Razzari, David Beljonne,* Paolo Samorì,* and Emanuele Orgiu*

Charge transport in organic semiconductors is notoriously extremely sensitive to the presence of disorder, both internal and external (i.e., related to interactions with the dielectric layer), especially for n-type materials. Internal dynamic disorder stems from large thermal fluctuations both in intermolecular transfer integrals and (molecular) site energies in weakly interacting van der Waals solids and sources transient localization of the charge carriers. The molecular vibrations that drive transient localization typically operate at low-frequency (<a-few-hundred cm^{-1}), which makes it difficult to assess them experimentally. Hitherto, this has prevented the identification of clear molecular design rules to control and reduce dynamic disorder. In addition, the disorder can also be external, being controlled by the gate insulator dielectric properties. Here a comprehensive study of charge transport in two closely related n-type molecular organic semiconductors using a combination of temperature-dependent inelastic neutron scattering and photoelectron spectroscopy corroborated by electrical measurements, theory, and simulations is reported. Unambiguous evidence that ad hoc molecular design enables the electron charge carriers to be freed from both internal and external disorder to ultimately reach band-like electron transport is provided.

1. Introduction

High charge carrier mobility is a prerequisite to ensure efficient electronic devices, such as field-effect transistors (FETs), solar cells, and light-emitting diodes.[1,2] The charge carrier mobility in organic semiconductors results from the interplay of a complex set of physical parameters related to morphology, energetic and structural disorder, and defects, which ultimately are all intimately related the molecular chemical structure.[3] When resorting to organic molecular materials with high degree of crystallinity, the effects of morphology and defects on charge transport are minimized, providing tools to single out the role of disorder. A primary source of disorder is internal and stems from large thermal fluctuations of (diagonal) site energies and, mostly, the (off-diagonal) intermolecular interactions mediating transport.[4]

Dr. M.-A. Stoeckel, Dr. M. Gobbi,[+] Prof. P. Samorì, Prof. E. Orgiu
Université de Strasbourg
CNRS
ISIS UMR 7006
8 allée Gaspard Monge, Strasbourg 67000, France
E-mail: samori@unistra.fr; emanuele.orgiu@emt.inrs.ca
Prof. Y. Olivier,[++] Dr. D. Dudenko, Dr. V. Lemaur, Dr. D. Beljonne
Laboratory for Chemistry of Novel Materials
University of Mons
Place du Parc, 20, Mons B-7000, Belgium
E-mail: david.beljonne@umons.ac.be
Dr. M. Zbiri
Institut Laue-Langevin
71 Avenue des Martyrs, Grenoble 38000, France

The ORCID identification number(s) for the author(s) of this article can be found under https://doi.org/10.1002/adma.202007870.

[+]Present address: CIC nanoGUNE BRTA, San Sebastian, 20018, Spain and IKERBASQUE, Basque Foundation for Science, Bilbao, 48013, Spain
[++]Present address: Unité de Chimie Physique Théorique et Structurale (UCPTS) & Laboratoire de Physique du Solide (LPS), Namur Institute of Structured Matter (NISM), University of Namur, Namur, Belgium

Dr. A. A. Y. Guilbert
Centre for Plastic Electronics and Department of Physics
Blackett Laboratory
Imperial College London
London SW7 2AZ, UK
Dr. G. D'Avino
Grenoble Alpes University
CNRS Grenoble INP, Institut Néel
25 rue des Martyrs, Grenoble 38042, France
Dr. F. Liscio, Dr. A. Migliori, Dr. L. Ortolani
CNR – IMM Sezione di Bologna
Via P. Gobetti 101, Bologna 40129, Italy
Dr. N. Demitri
Elettra – Sincrotrone Trieste
S.S. 14 Km 163.5 in Area Science Park, Basovizza, Trieste I-34149, Italy
Dr. X. Jin, Dr. Y.-G. Jeong, Prof. L. Razzari, Prof. E. Orgiu
Institut National de la Recherche Scientifique
Centre Énergie Matériaux Télécommunications
1650 Blv. Lionel-Boulet, Varennes, Québec J3X 1S2, Canada
Dr. A. Liscio
CNR – Institute for Microelectronic and Microsystems (IMM) Section of Roma-CNR
Via del fosso del cavaliere 100, Roma 00133, Italy

**ADVANCED
SCIENCE NEWS**

www.advancedsciencenews.com

**ADVANCED
MATERIALS**

www.advmat.de

The other source of disorder for charge carriers in FETs is external, and it arises from the coupling of charge carriers to substrate phonons and randomly oriented dipoles at the semiconductor/gate dielectric interface.[5–7] External disorder was invoked in previous reports as a key limiting factor to charge delocalization.[7] In spite of the above-mentioned internal and external sources of disorder owing to the noncovalent and weak nature of the forces holding together such van der Waals solids, several highly-performing molecular organic single crystals were found to exhibit band-like transport near room temperature.[8–11] When properly supported by Hall measurements, the latter transport regime indicates that electron wave functions can be delocalized over several molecular units.[11,12] Although the sole standard electrical FET characterization is not capable of measuring the extent of charge delocalization, the band-like transport is usually invoked when the temperature dependence of the field-effect mobility (μ_{FET}) resembles that observed in inorganic semiconductors, such as silicon, i.e., showing an increase in μ_{FET} upon cooling down from room temperature.

Hence, one can confidently conclude that the combination of internal and external disorder ultimately dictates the extent of charge delocalization in crystalline molecular semiconductors. However, hitherto these two disorder components could never be disentangled. In addition, there is still considerable controversy as to which degree can a carrier wave function extend over neighboring molecules and especially how this is directly linked to the molecular structure.

Here we use two different perylene diimide (PDI) derivatives as model systems to disentangle the role of the internal versus external disorder on electron transport in organic crystals. Through a systematic structural, electrical, and spectroscopic characterization combining field-effect transistor devices, inelastic neutron scattering, and low-wavenumber spectroscopy measurements together with numerical simulations, we were able to single out the most important vibrational lattice modes (for charge transport) of both PDI single crystals and to correlate them with the molecular chemical structure.

The two PDI derivatives (whose chemical structure is portrayed in **Figure 1**a,b) are functionalized with cyano groups in the bay-region and feature similar environmental stability.[13–16] They only differ by the lateral chain on the imide position, initially designed to enhance their solubility. The first derivative, *N-N′*-bis(n-octyle)-(1,7&1,6)-dicyanoperylene-

3,4:9,10-bis(dicarboximide) known as PDI8-CN$_2$, bears an alkyl chain on each side,[17] while its fluorinated derivative, *N-N′*-bis(heptafluorobutyl)-(1,7&1,6)-dicyanoperylene-3,4:9,10-bis(dicarboximide) also called as PDIF-CN$_2$, exposes a fluorinated one.[18,19]

2. Results and Discussion

Solution-processed single crystals were grown by means of solvent induced precipitation (SIP) (see Supporting Information) in order to obtain thin crystals with a reduced number of step edges, which have been found to be detrimental for charge transport.[20] In addition, such a crystal growth method makes it unfavorable for solvent molecules to get incorporated in the final crystal. Once formed, the crystals were then drop-casted on an octadecyl trichlorosilane (OTS)-treated SiO$_2$ substrate. The OTS functionalization acts as a molecular spacer that separates the dielectric surface from the PDI molecules sitting atop. More specifically, such dielectric treatment allows to decrease the coupling between the conjugated electron-transporting part of the molecules and the dielectric[7] and to prevent the presence of silanol groups at the interface of the surface that act as traps for electrons.[21] Two electrodes were evaporated through a shadow mask (Figure S5, Supporting Information) to form the final bottom-gate top-contact field-effect transistors (Figure 1c,d,g). With this approach, we fabricated top-contact bottom-gate single-crystal FET whose contacts were thermally evaporated through a shadow masks. The latter fabrication step avoids contamination resulting from chemical residues of photoresist and its developer, which may occur when using a standard lithographic process (Figure S6, Supporting Information). Furthermore, the dielectric functionalization (operated by functionalizing SiO$_2$ with OTS) allowing to disentangle external versus internal disorder effects on the electrical transport characteristics can only be employed in a bottom-gate architecture. In addition, the lateral chains acting as a spacer make such contributions negligible for PDI derivatives, while this has been attributed as the possible culprit for band-like transport not being observed in pentacene and sexithiophene single crystal FETs.[11] As confirmed by structural characterization, the conjugated core-dielectric distance is nearly identical in both PDIs, which also allows to consider nearly identical the amount of external disorder the two types of molecules are subjected to. Furthermore, PDI8-CN$_2$ and PDIF-CN$_2$ crystals were drop-casted on an OTS layer, which further ensures a minimization of the substrate-induced external disorder.

Both compounds, when integrated into FET structures, present ideal n-type characteristics with reliability factors close to 100% for both PDI compounds, while keeping low maximum power densities and maximum current densities below 4 W cm^{-2} and 26 A cm^{-2}, respectively (Table S1, Supporting Information),[22] with mobility values for PDIF-CN$_2$ being larger than for PDI8-CN$_2$ by about one order of magnitude over the temperature range investigated (Figure 1f,i). The trend of the temperature-dependent mobility (Figure 1f) suggests band-like transport in PDIF-CN$_2$, as previously confirmed by Hall measurements.[7] This behavior could be generally observed in high-purity crystals and it is generally accompanied

Dr. M.-V. Nardi
Istituto dei Materiali per l'Elettronica ed il Magnetismo
IMEM-CNR
Sezione di Trento
Via alla Cascata 56/C, Povo, Trento 38100, Italy
Prof. L. Pasquali
Istituto Officina dei Materiali
IOM-CNR
s.s. 14, Km. 163.5 in AREA Science Park, Basovizza, Trieste 34149, Italy
Prof. L. Pasquali
Dipartimento di Ingegneria E. Ferrari
Università di Modena e Reggio Emilia
via Vivarelli 10, Modena 41125, Italy
Prof. L. Pasquali
Department of Physics
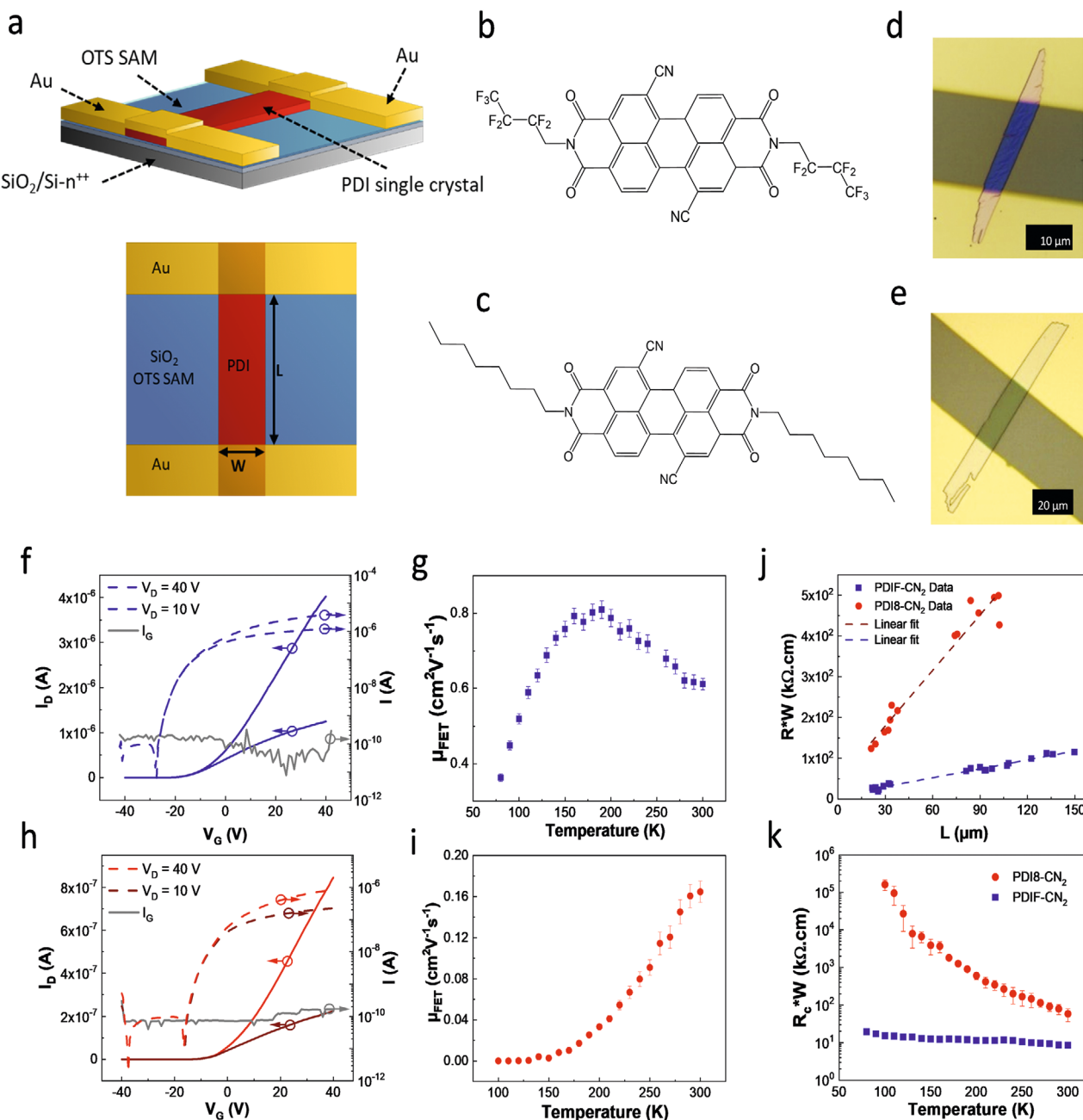University of Johannesburg
PO Box 524, Auckland Park 2006, South Africa

ADVANCED
SCIENCE NEWS
www.advancedsciencenews.com

ADVANCED
MATERIALS
www.advmat.de

Figure 1. Temperature-dependent electrical characterization of PDI-based devices. a) Schematics of a device based on PDI single crystal, 3D, and top view. b) Chemical structure of PDIF-CN$_2$. c) Chemical structure of PDI8-CN$_2$. d) Optical microscopy image of a PDIF-CN$_2$ single-crystal FET. f) Transfer curve of a single-crystal FET of PDIF-CN$_2$ with $V_D = 10$ V (in dark blue) and $V_D = 40$ V (in blue). The gate current is plotted in gray. g) Evolution of the linear mobility of a representative PDIF-CN$_2$ single crystal as a function of temperature, exhibiting band-like behavior. e) Optical image of a PDI8-CN$_2$ single-crystal FET. h) Transfer curve of a PDI8-CN$_2$ single-crystal FET with $V_D = 10$ V (in dark red) and $V_D = 40$ V in red. i) Evolution of the linear mobility of a representative PDI8-CN$_2$ sample as a function of temperature, revealing thermally activated transport. j) Transmission-line method curves for both PDIF-CN$_2$ and PDI8-CN$_2$ recorded on multiple devices at 300 K, and k) evolution of the contact resistance of both compounds as a function of temperature.

by an experimental trend of mobility, i.e., $\frac{\partial \mu}{\partial T} < 0$, when charge carrier mobility is not drain-bias dependent.[23,24] Below a given temperature, typically ranging between 180 and 220 K, the transport follows again a thermally activated mechanism. This is expected since, at such low temperatures, charge transport properties deviate from the ideal behavior predicted

computationally in ref. [25] for defect-free single crystals and instead become dominated by scattering with, and trapping to, defects, as, e.g., line (dislocations) or surface (stacking faults) defects. The study of the detailed nature of these defects and how these affect the charge-carrier mobility is beyond the scope of this work. The value of room-temperature mobility measured on a

representative statistics of PDIF-CN$_2$ single crystals, approaching 1 cm^2 V^{-1} s^{-1}, is very close to previously reported mobility values ($\approx$2 cm^2 V^{-1} s^{-1}) measured on an insulator with a dielectric permittivity (PMMA, $\varepsilon_r \approx 4$) similar to that of our dielectric (SiO$_2$, $\varepsilon_r = 3.9$).[11] However, in few instances, room temperature mobilities 2 cm^2 V^{-1} s^{-1} were also achieved in a previous report on the very same crystals.[26] The apparent mobility mismatch may arise from the high value of the dielectric permittivity employed in our study.[27] Regarding PDI8-CN$_2$ (Figure 1i), the transport seems to follow a purely thermally-activated behavior over the whole measured temperature range (80–300 K). The same electrical behavior for both derivatives was observed also when a thin insulating layer of divinyl-tetra-methyldisiloxane-bis (benzocyclobutene) (BCB), replacing the chemisorbed OTS SAM, was spin-cast on SiO$_2$ (Figures S15 and S16, Supporting Information). Since the transport measurements on both PDI derivatives were carried out in three-terminal devices, the contact resistance was determined at each of temperature value at which the mobility was measured (through a classical transmission line method) and the curves corrected accordingly (Figure S12, Supporting Information). It is noteworthy that no hysteresis in mobility was observed upon heating and cooling the devices during the measurement (Figure S14, Supporting Information). The contact resistance, extracted by following the transmission-line method on single-channel devices integrating crystals of comparable thicknesses (Figure S11, Supporting Information) was found to be larger in PDI8-CN$_2$ than in PDIF-CN$_2$ devices. This finding is fully consistent with the characterization performed by means of electron energy loss spectroscopy (EELS) and ultraviolet photoelectron spectroscopy (UPS) (Figure 2) in single crystals, being therefore fully comparable with the device case, which uses single crystals as the active layer. In particular, EELS measurements of the optical bandgap (E_{opt}) of the crystals of both compounds provided nearly identical values for PDI8-CN$_2$ and PDIF-CN$_2$. While E_{opt} and presumably the electronic bandgap (the highest occupied molecular orbital (HOMO) the lowest unoccupied molecular orbital (LUMO)) of PDI8-CN$_2$ and PDIF-CN$_2$ are nearly equivalent, their respective ionization energies were found to be offset by as much as 0.70 eV (amounting to 7.9 and 7.4 eV, for PDIF-CN$_2$ and PDI8-CN$_2$, respectively). Considering the measured energy difference between E_F and HOMO level (Figure 2c), it appears clear that electron injection is certainly more favorable in PDIF-CN$_2$ thanks to the reduction of the energy barrier between Au work function and its LUMO. Structural analysis on the crystals confirmed the bulk structure, slipped-stacked for PDI8-CN$_2$, and brick-wall for PDIF-CN$_2$ (**Figure 3**a–f), with only one molecule per primitive cell, which is uncommon for small molecule semiconducting materials.[1,28,29]

To rule out any possible phase transition upon temperature, we performed temperature-dependent structural characterizations (Figure 3g,h; and Section S4, Supporting Information) and temperature-dependent solid-state F-NMR (Figures S23 and S24, Supporting Information) on the fluorine atoms. No significant structural changes (phase transitions) were observed with both techniques upon varying the temperature of the measurement. Thus, we are confident that the observed charge transport behaviors are not driven by any structural change, as it is the case, for example, with tetracene.[30,31]

In order to analyze internal static disorder generated by the presence of trap states in the bulk of the crystals, the trap density was extracted in both compounds in the framework of the space-charge limited current (SCLC) analysis (Figure S17, Supporting Information).[32,33] While the absolute value of trap density when extracted through SCLC can sometimes be underestimated, we used this method to compare the ratio of trap density between PDIF-CN$_2$ and PDI8-CN$_2$ single crystals. PDI8-CN$_2$ crystals were found to exhibit a trap bulk density (3×10^{12} cm^{-3}) comparable to that of PDIF-CN$_2$ crystals (1×10^{13} cm^{-3}). Our crystals exhibit bulk trap densities which are lower or comparable to those of previously reported vapor-grown single crystals of rubrene ($N_t \approx 10^{15}$ cm^{-3}),[33] pentacene ($N_t \approx 10^{11}$ cm^{-3}),[34] tetracene ($N_t \approx 10^{13}$ cm^{-3}),[31] and solution-grown hydroxycyanobenzene ($N_t \approx 10^{13}$ cm^{-3}) single crystals[35] measured through SCLC measurements. However, since in bottom-gate FET devices the charge transport is known to occur within the first nanometers at the interface with the dielectric, a deeper analysis of
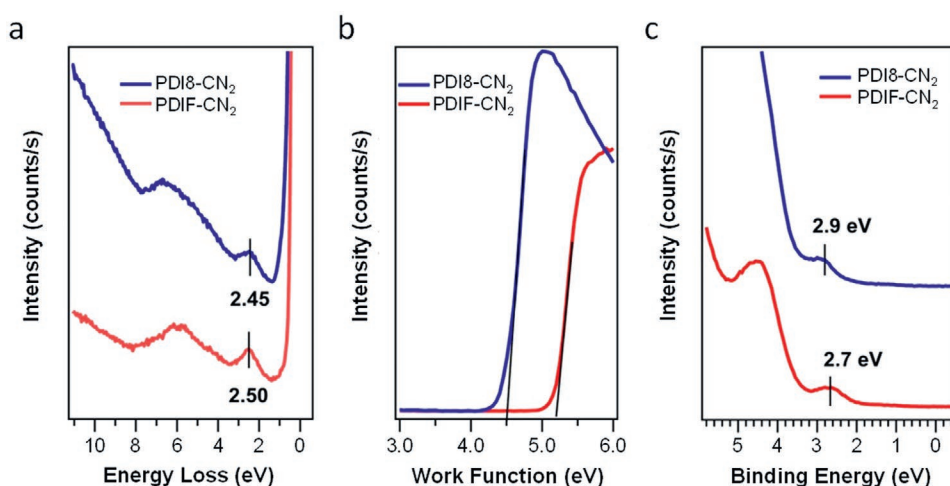

Figure 2. Energy levels of PDIF-CN$_2$ and PDI8-CN$_2$. a) EELS spectra of PDIF-CN$_2$ and PDI8-CN$_2$. The marked values in the experimental traces represent the energy difference between the primary beam and the energy of the first loss structure, i.e., the optical bandgap (E_{opt}). E_{opt} corresponds to 2.50 eV for PDIF-CN$_2$ and 2.45 eV for PDI8-CN$_2$. b,c) Work function and E_F – HOMO measurements for PDIF-CN$_2$ and PDI8-CN$_2$, respectively.
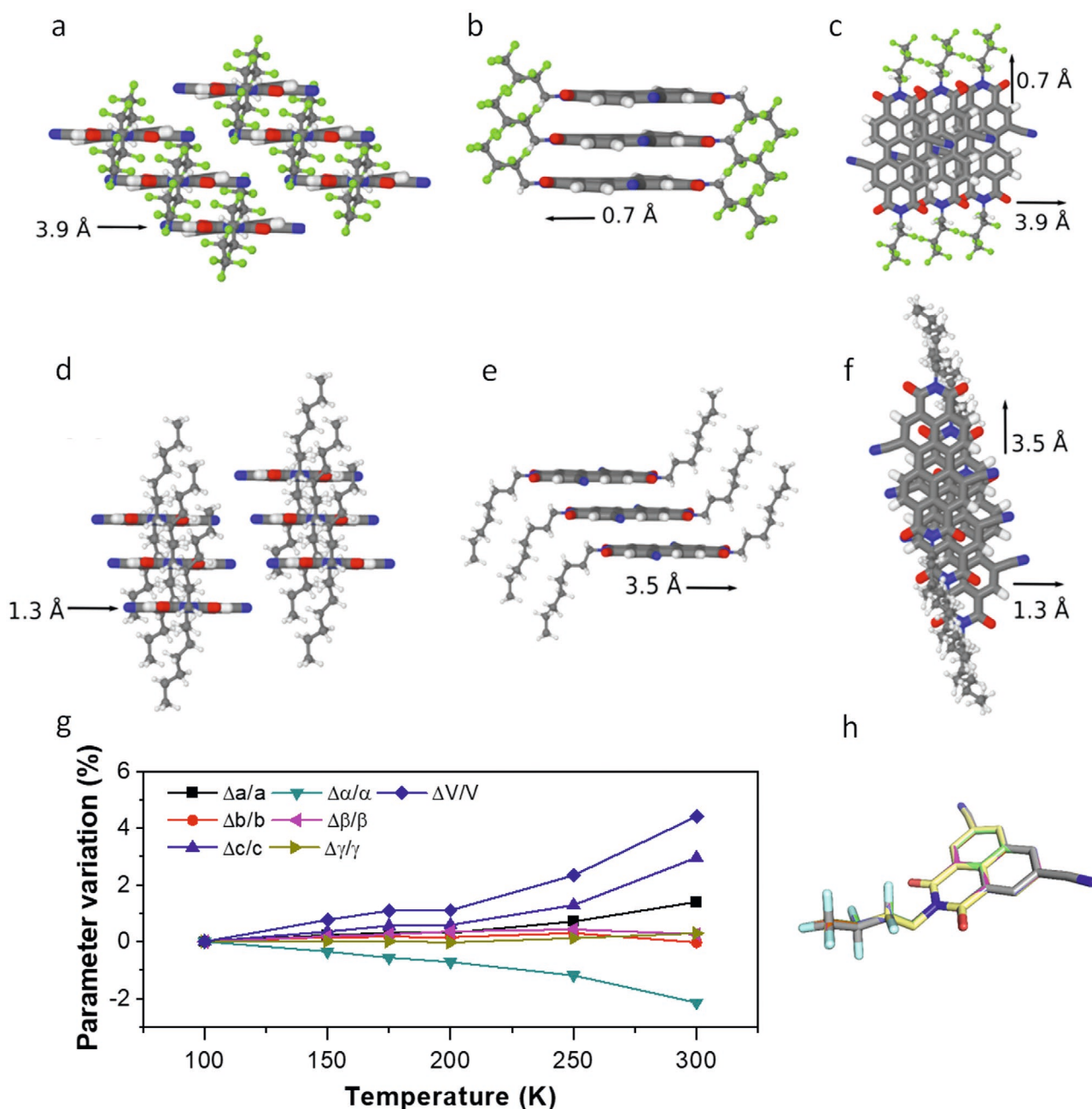
Figure 3. Structural properties of PDIF-CN$_2$ and PDI8-CN$_2$. a–c) Side view and top view packing of PDIF-CN$_2$. d–f) Side view and top view packing of PDI8-CN$_2$. g) Variation of the lattice parameter a, b, c, α, β, γ, and volume (V) during the thermal annealing of PDIF-CN$_2$ single crystals where strongest variation was the expansion by 3% of the *c*-axis at 300 K, which lead the volume to increase by 4.4%, which is not indicative of an actual phase transition. h) Overlap of equivalent PDIF-CN$_2$ conformations found in 100–300 K models (R.M.S.D. between models < 0.05 Å). Hydrogens omitted for clarity.

the electron trapping is required to probe the crystal surface. In particular, step edges at the surface of single crystals were found to trap electrons in both p-type and n-type organic semiconductor crystals.[20] In particular, charge carrier mobilities would decrease with increasing step density. Interestingly, the same study also showed that the thickness of the crystals can influence the type of transport, which can go from thermally activated, in very thick crystals (>30 μm thick), to band-like transport, in thinner crystals (≈5 μm thick). This former experimental observation agrees well with the suggested relationship

of proportionality between thickness and density of step edges. More specifically, in the case of PDIF-CN$_2$, the authors demonstrated that charge carrier mobility increases with decreasing the step density. Our atomic force microscopy (AFM) measurements carried out on the surface of the very same crystals that were electrically probed in the devices, revealed that the typical thickness of both PDIF-CN$_2$ and PDI8-CN$_2$ crystals falls between 100 and 200 nm. For both derivatives, no step edges were measured on the crystals' surface as revealed by means of Kelvin probe force microscopy (KPFM—see

**ADVANCED
SCIENCE NEWS**
www.advancedsciencenews.com

**ADVANCED
MATERIALS**
www.advmat.de

Section S5, Supporting Information). In this regard, our experimental observation is in line with the discussions by He et al. indicating that thin crystals exhibit minimal static disorder thanks to the absence of step edges at which electrons could be trapped. This further experimental evidence allows to state more soundly that the significant differences in transport regimes observed in our molecular systems do not stem from a difference in bulk or surface trap density but should be sought after in the intrinsic (internal) dynamic disorder behavior. Provided that the relevant time scale for charge motion is substantially shorter than the intermolecular vibrational time, charge carriers do transiently (de)localize in space. Hence, the frequency of the intermolecular vibrations is a crucial parameter. In particular, low-frequency (<200 cm^{-1}) large-amplitude vibrations or vibrations displaying strong local and nonlocal electron–phonon coupling constants are those mostly hampering efficient charge transport.[36]

In order to investigate the charge localization degree of both PDI derivatives, we have performed atomistic calculations of the time-dependent electronic structure of the two molecular crystals by means of a combined classical/quantum modeling approach.[37] Computational details are provided in the Supporting Information. In a nutshell, we first ran molecular dynamics (MD) simulations to sample the thermal lattice motion and to compute, as a function of time, the microscopic parameters governing the electron transport in both PDI derivatives. This includes intermolecular charge transfer integrals and molecular site energies, the latter explicitly accounting for supramolecular electrostatic interactions that largely contribute to energetic disorder.[38] We then fed this atomistic information into a tight-binding model for electron states in the 2D high-mobility planes, in order to obtain the localization length (thermally averaged inverse participation ratio) of electron carriers as a function of time.

The results of the hybrid classical/quantum calculations shown in **Figure 4**a point to a transient (de)localization of the electron wave function that breathes around average values of ≈ 11 molecules in PDIF-CN$_2$ compared to only ≈ 4 molecules in PDI8-CN$_2$. The large averaged spatial extent of the electron carrier in PDIF-CN$_2$ as opposed to that of PDI8-CN$_2$ suggests a remarkably higher tendency of the carriers to be delocalized in the fluorinated compound. This is a direct consequence of the crystalline packing of both derivatives, being slipped-stack for PDI8-CN$_2$ but brick-wall for PDIF-CN$_2$, as evidenced by the transfer integral distributions in Figure S28 (Supporting Information).

In order to gain a deeper understanding on the different charge transport mechanisms observed on PDI derivatives, we measured the low-frequency vibrations of both compounds. We employed temperature-resolved inelastic neutron scattering (INS) in combination with modeling and simulations. INS makes it possible to explore quantitatively phonon dynamics over the whole Brillouin zone, without being subjected to any specific constraint of selection rules. Unlike very recent works[39,40] based on low-temperature Stokes INS spectra measurements providing insight into molecular vibrations (internal modes), in the present study we used cold-neutron time-of-flight spectroscopy (see Section S8 in the Supporting Information), in order to measure in the up-scattering regime the anti-Stokes phonon modes (external modes) with a high-energy resolution and an excellent signal-to-noise ratio. Therefore, the low-frequency vibrations (up to 600 cm^{-1}) covering both crystal lattice modes (phonons or external modes)

and some of the subsequent low-frequency molecular vibrations (internal modes) can be mapped out properly, allowing to study their temperature-dependence (150–300K) with direct implications on charge transport (Figure 4b,c). In the case of PDI8-CN$_2$, the vibrational peaks become more resolved upon lowering the temperature. This is expected due to a reduction of the thermally-induced displacements, related to the Debye–Waller factor, leading to less broadened features in inelastic neutron scattering. Interestingly, for PDIF-CN$_2$, upon cooling, some low-energy modes below 250 cm^{-1} become clearly distinguishable, exhibiting a pronounced temperature-dependence, seemingly triggering/inducing other effects beyond (or in addition to) the expected reduction of thermal displacements. Further, a new vibrational feature appears at 545 cm^{-1} in the generalized density of states (GDOS).[41] It must be emphasized here that the INS-based GDOS spectra are dominated by the dynamical degrees of freedom of hydrogen atoms, being the strongest neutron scatterers in PDIF-CN$_2$ and PDI8-CN$_2$. Hydrogens are located on the core of the materials in PDIF-CN$_2$ and both on the core and side chains in PDI8-CN$_2$. Therefore, INS intensities of the two PDIs are, in principle, not directly comparable. To underpin our INS measurements, we calculated the INS spectra by Fourier transform of the velocity autocorrelation functions, dissecting the contribution from individual elements along the MD trajectory. The partial contributions had to be neutron-weighted to obtain the GDOS spectra.[40] MD[42] simulations are found to be in a good agreement with the experimental INS spectra by applying a frequency scaling factor of 0.84 and 0.75 for PDI8-CN$_2$ and PDIF-CN$_2$, respectively (Figure 4d,e). Furthermore, the partial contributions show that the peak around 200 cm^{-1} stems from the nitrogen contribution (Figure S35, Supporting Information), with its intensity being larger in the case of PDI8-CN$_2$, and this is also reflected in the room-temperature THz spectroscopy spectrum (Figure S37, Supporting Information). Carbon atoms form the host lattice to which the other atoms are bond. Therefore, their dynamical contribution reflects the main lattice vibration in terms of frequency spread. The calculated partial density of states of carbons highlight a stronger intensity of phonons for PDI8-CN$_2$ as compared to PDIF-CN$_2$, up to 192 cm^{-1} (Figure S36, Supporting Information). By combining INS with MD simulations, as shown in Figure 4d,e, it was possible on the one hand to validate the force field, and on the other hand to get a deeper insight into the partial lattice dynamical contributions. This enabled us to ultimately compare the INS intensities of the two PDIs.

As our model was able to reproduce quite confidently the whole vibrational modes measured by INS, we next proceeded with the calculation of the electron–phonon coupling spectral density for the transfer integrals along the π–π direction (see **Figure 5**a), as the temperature dependence is expected to be mainly sourced by nonlocal electron–phonon coupling along the dominant transport pathway. Results obtained for the off-diagonal coupling along the π-edge (see Figure S31, Supporting Information) direction as well as for the site energies (Figure S32, Supporting Information) are reported. We note that the intense peak around 400 cm^{-1} for PDI8-CN$_2$ is also observed in the electron–phonon coupling spectrum of the site energies (see Figure S30, Supporting Information).

These computed spectra convincingly show that low-energy (<200 cm^{-1}) phonons are much more strongly coupled to the electronic degrees of freedom along the π–π direction in PDI8-CN$_2$ compared to PDIF-CN$_2$ (Figure 5b), thereby rationalizing

**ADVANCED
SCIENCE NEWS**

www.advancedsciencenews.com
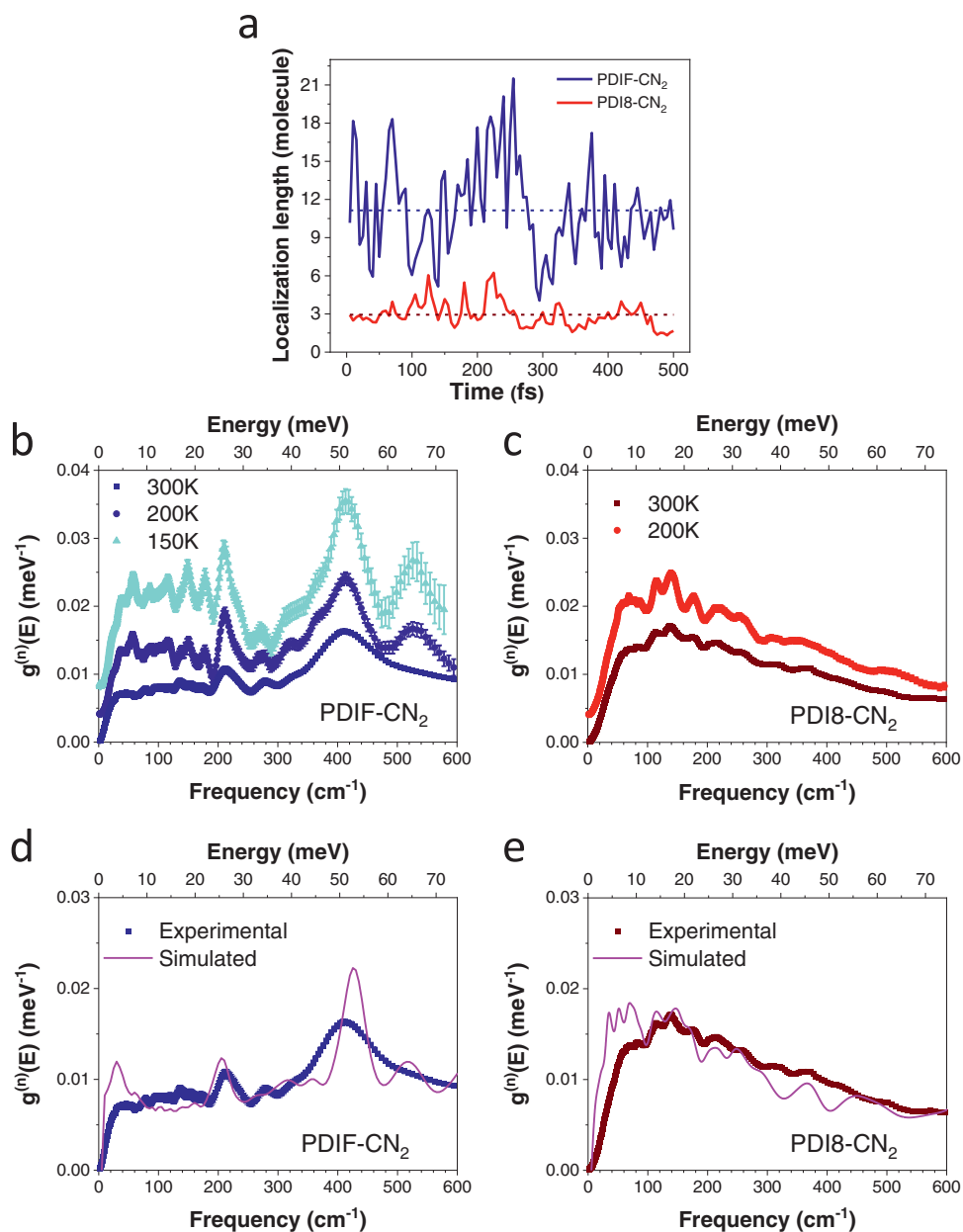
**ADVANCED
MATERIALS**

www.advmat.de

Figure 4. Experimentally determined and calculated vibrational modes of PDIF-CN$_2$ and PDI8-CN$_2$. a) Localization length over time from quantum/classical simulations: charge carriers are delocalized over ≈11 PDIF-CN$_2$ molecules (in blue). Conversely, charge carriers are localized only over ≈4 molecular units in the case of PDI8-CN$_2$ (in red). b,c) Temperature-dependent inelastic neutron scattering spectra in terms of the GDOS of PDIF-CN$_2$ and PDI8-CN$_2$, respectively. (Full GDOS spectra resolved in temperature shown in Figure S33, Supporting Information). d,e) Comparative experimental-simulated INS-based GDOS spectra of PDIF-CN$_2$ and PDI8-CN$_2$, respectively (room temperature). The GDOS have been shifted for convenience.

the more pronounced trend toward breaking of the translational symmetry and spatial confinement of the electrons in the former molecule. The more pronounced intensity of the phonon spectra for PDI8-CN$_2$ was experimentally proved also by room-temperature THz spectroscopy (Figure S37, Supporting Information), which allows an immediate and quantitative comparison between the two PDI derivatives. In PDI8-CN$_2$, such low-energy phonons modulate the wave function overlap as a result of a combination of mostly short-axis translations and rotations[43,44] changing the distance and orientation along the packing direction (see Supporting Information for detailed

assignment), thereby largely affecting the magnitude of the transfer integrals (in contrast with longitudinal displacements). The large (small) relative thermal molecular motions predicted for PDI8-CN$_2$ (PDIF-CN$_2$), as reported in Table S3 (Supporting Information), translate into broad (narrow) distributions in transfer integrals (Figure S28, Supporting Information). Altogether, similar to didodecyl-benzothienobenzothiophene (BTBT) derivatives[45] and in contrast to the slipped-stack crystal organization of PDI8-CN$_2$, the brick-wall crystal organization in PDIF-CN$_2$ conveys both large electronic interactions and a smaller sensitivity to thermal energetic disorder that act in
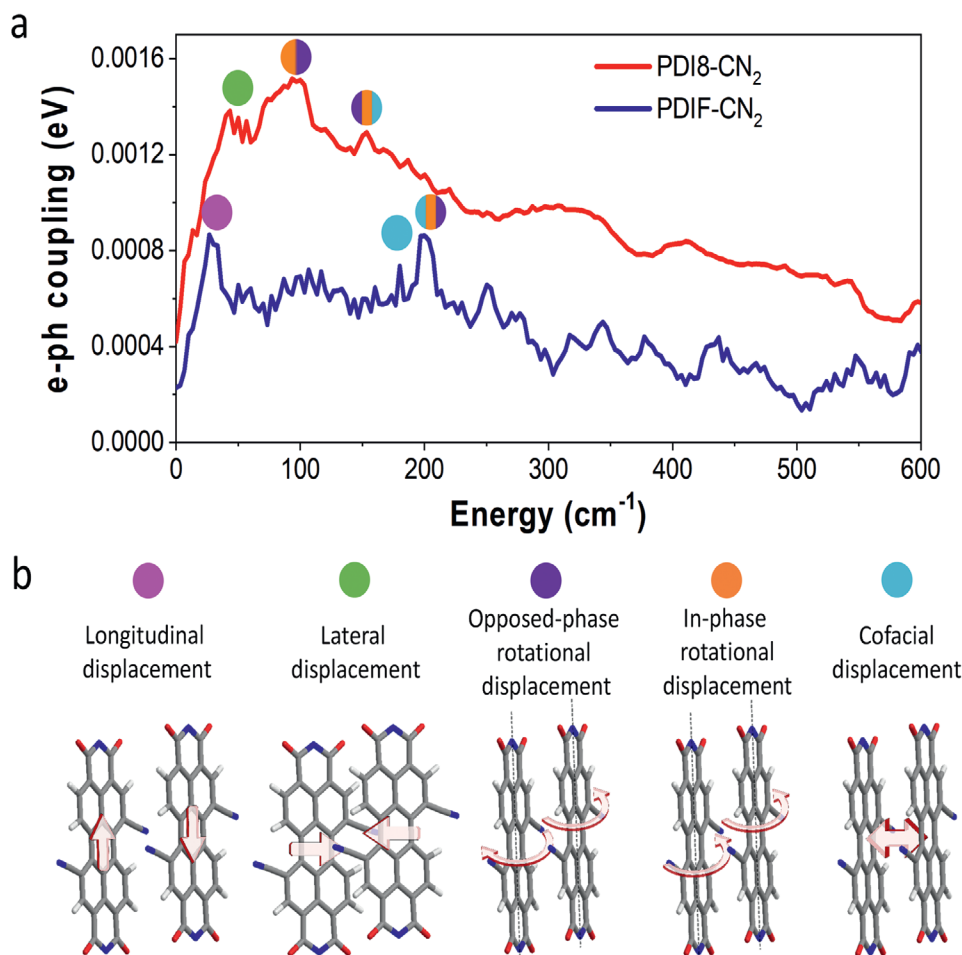
Figure 5. Electron–phonon coupling analysis and assigned molecular displacement for PDI8-CN$_2$ and PDIF-CN$_2$. a) Electron–phonon coupling spectrum of the time-dependent transfer integrals along the π–π direction in crystals of PDI8-CN$_2$ (in red) and PDIF-CN$_2$ (in blue), respectively ($T = T_{amb}$). b) Different molecular displacements and related color code associated to the spectra in (a).

concert to delocalize the charge carriers, hence triggering band-like transport.

3. Conclusion

In summary, our systematic and comparative investigation of electron transport in single crystals based on PDI derivatives with subtle difference in the side chains revealed the existence of markedly different charge transport mechanisms, i.e., band-like versus thermally activated transport. The careful design of our experimental work allowed to experimentally disentangle the effect of external versus internal (intrinsic) disorder, and to focus on the relationship between the latter and the observed band-like transport through a number of (temperature-resolved) techniques. In particular, charge transport in PDIF-CN$_2$ and PDI8-CN$_2$ was analyzed through temperature-dependent electrical and structural characterization, corroborated by THz spectroscopy and by temperature-dependent inelastic neutron scattering. Our findings are also backed by a sound and fine atomistic modeling, which revealed a more pronounced degree of wave function delocalization for PDIF-CN$_2$ as a result of lower electron–phonon coupling. The experimentally observed

differences in transport mechanism between band-like for PDIF-CN$_2$ and thermally activated transport for PDI8-CN$_2$ can be ascribed to the different phononic activity at low wavenumber, as evidenced by electron–phonon coupling calculations. These calculations show that intrinsic (internal) dynamic disorder builds up in a qualitatively different way in brickwall and slipped-stacked PDI derivatives with respect to herringbone lattices of elongated molecules (e.g., pentacene, BTBT, etc.). While in the latter case long-axis intermolecular displacements (below 50 cm^{-1}) provide a largely dominant contribution the total energetic disorder,[40] we have revealed here that the scenario is more complex for PDI, with several modes (up to 200 cm^{-1}, including short-axis translation and rotations) coming into play. As such, our work suggests rational molecular design guidelines for high mobility (n-type) molecular semiconductors: a combined effect of translations and rotations along the short molecular axis gives rise to low-wavenumber phonons capable of modulating the electron wave function overlap and to affect the magnitude of the transfer integrals in a much more pronounced manner than molecular longitudinal displacements. This study suggests that a general strategy to hinder low frequency phonons can involve the functionalization of the lateral chains with fluorocarbon groups whose interactions are stronger than based on simple

**ADVANCED
SCIENCE NEWS**

www.advancedsciencenews.com

**ADVANCED
MATERIALS**

www.advmat.de

methylation approaches. Such a stronger interaction between $-CF_3$ versus $-CH_3$ groups can lead to a selective locking of thermal lattice fluctuations below few hundred cm^{-1}. We anticipate that an adequate lateral functionalization with fluorocarbons chains along the short axis of brickwall and slipped stack molecular semiconductors (such as indenofluorene[46] or bithiophene-benzothiazole structures[47]) may result into a stiffening of the translational and rotational phonons, leading to smaller amplitude motion at room temperature and therefore a higher degree of delocalization of the electron wavefunction. While providing a limited set of design rules to achieve the highest degree of electron delocalization in organic semiconductors remains far from trivial, our experimental results coupled with simulations suggests that n-type semiconductors with low-wavenumber phonons associated to short-axis translation generate large energetic disorder. These considerations will therefore help the design of better next-generation electronics materials.

Although this work puts forward the importance of controlling vibrational dynamics through molecular design for electron charge transport in organic FETs, studying and engineering phonons in organic semiconductors is also key for exciton separation in organic photovoltaics and the control of heat transport in organic-based thermoelectrics.

4. Experimental Section

X-ray Diffraction Traces as a Function of Temperature: CCDC 1848556, 1848559, 1848555, 1848558, 1848557, and 1848554 contain the supplementary crystallographic data for compounds PDIF-CN$_2$ at 100, 150, 175, 200, 250, and 300 K. These data can be obtained free of charge from The Cambridge Crystallographic Data Centre via https://www.ccdc.cam.ac.uk/structures.

Supporting Information

Supporting Information is available from the Wiley Online Library or from the author.

Author Contributions

M.-A.S. and Y.O. contributed equally to this work. D.B. is a FNRS Research Director. E.O. conceived the research. E.O., P.S., and D.B. supervised the work. M.-A.S. fabricated the devices and performed the electrical measurements under the guidance of M.G. and E.O. M.-A.S. carried out the solid-state NMR measurements. Y.O., D.D., V.L., and G.D. performed the simulations. A.A.Y.G. and M.Z. conceived the neutron scattering study, wrote the neutron beamtime proposal, carried out the INS experiments, treated and analyzed the data and assisted with data interpretation. F.L. and N.D. carried out the XRD experiments and analyzed the data. F.L., A.M., and L.O. carried out the cryogenic SAED experiments and analyzed the data. A.L. carried out the SPM measurements and analyzed the data. M.V.N. and L.P. performed the UPS and EELS measurements and analyzed the data. X.J., Y.-G.J., and L.R. carried out the THz measurements and analyzed the data. E.O., M.-A.S., and P.S. wrote the manuscript and all authors participated in manuscript preparation and editing.

Conflict of Interest

The authors declare no conflict of interest.

Data Availability Statement

The data that support the findings of this study are available from the corresponding author upon reasonable request.

[1] O. Ostroverkhova, *Chem. Rev.* **2016**, *116*, 13279.
[2] H. Sirringhaus, *Adv. Mater.* **2014**, *26*, 1319.
[3] G. Schweicher, Y. Olivier, V. Lemaur, Y. H. Geerts, *Isr. J. Chem.* **2014**, *54*, 595.
[4] A. Troisi, G. Orlandi, *Phys. Rev. Lett.* **2006**, *96*, 086601.
[5] T. Richards, M. Bird, H. Sirringhaus, *J. Chem. Phys.* **2008**, *128*, 234905.
[6] I. N. Hulea, S. Fratini, H. Xie, C. L. Mulder, N. N. Iossad, G. Rastelli, S. Ciuchi, A. F. Morpurgo, *Nat. Mater.* **2006**, *5*, 982.
[7] N. A. Minder, S. Lu, S. Fratini, S. Ciuchi, A. Facchetti, A. F. Morpurgo, *Adv. Mater.* **2014**, *26*, 1254.
[8] V. Podzorov, E. Menard, A. Borissov, V. Kiryukhin, J. A. Rogers, M. E. Gershenson, *Phys. Rev. Lett.* **2004**, *93*, 086602.
[9] V. Podzorov, E. Menard, J. A. Rogers, M. E. Gershenson, *Phys. Rev. Lett.* **2005**, *95*, 226601.
[10] J. Takeya, J. Kato, K. Hara, M. Yamagishi, R. Hirahara, K. Yamada, Y. Nakazawa, S. Ikehata, K. Tsukagoshi, Y. Aoyagi, T. Takenobu, Y. Iwasa, *Phys. Rev. Lett.* **2007**, *98*, 196804.

[11] N. A. Minder, S. Ono, Z. Chen, A. Facchetti, A. F. Morpurgo, *Adv. Mater.* **2012**, *24*, 503.

[12] T. Uemura, K. Nakayama, Y. Hirose, J. Soeda, M. Uno, W. Li, M. Yamagishi, Y. Okada, J. Takeya, *Curr. Appl. Phys.* **2012**, *12*, S87.

[13] B. A. Jones, A. Facchetti, M. R. Wasielewski, T. J. Marks, *J. Am. Chem. Soc.* **2007**, *129*, 15259.

[14] C. Huang, S. Barlow, S. R. Marder, *J. Org. Chem.* **2011**, *76*, 2386.

[15] M.-Y. Kuo, H.-Y. Chen, I. Chao, *Chem. – Eur. J.* **2007**, *13*, 4750.

[16] B. A. Jones, A. Facchetti, M. R. Wasielewski, T. J. Marks, *Adv. Funct. Mater.* **2008**, *18*, 1329.

[17] B. Yoo, T. Jung, D. Basu, A. Dodabalapur, B. A. Jones, A. Facchetti, M. R. Wasielewski, T. J. Marks, *Appl. Phys. Lett.* **2006**, *88*, 082104.

[18] B. A. Jones, M. J. Ahrens, M.-H. Yoon, A. Facchetti, T. J. Marks, M. R. Wasielewski, *Angew. Chem., Int. Ed.* **2004**, *43*, 6363.

[19] A. S. Molinari, H. Alves, Z. Chen, A. Facchetti, A. F. Morpurgo, *J. Am. Chem. Soc.* **2009**, *131*, 2462.

[20] T. He, Y. Wu, G. D'Avino, E. Schmidt, M. Stolte, J. Cornil, D. Beljonne, P. P. Ruden, F. Würthner, C. D. Frisbie, *Nat. Commun.* **2018**, *9*, 2141.

[21] L.-L. Chua, J. Zaumseil, J.-F. Chang, E. C.-W. Ou, P. K.-H. Ho, H. Sirringhaus, R. H. Friend, *Nature* **2005**, *434*, 194.

[22] H. H. Choi, K. Cho, C. D. Frisbie, H. Sirringhaus, V. Podzorov, *Nat. Mater.* **2017**, *17*, 2.

[23] T. Sakanoue, H. Sirringhaus, *Nat. Mater.* **2010**, *9*, 736.

[24] H. T. Yi, Y. N. Gartstein, V. Podzorov, *Sci. Rep.* **2016**, *6*, 23650.

[25] L. Wang, D. Beljonne, *J. Phys. Chem. Lett.* **2013**, *4*, 1888.

[26] W. Rekab, M.-A. Stoeckel, M. E.l Gemayel, M. Gobbi, E. Orgiu, P. Samorì, *ACS Appl. Mater. Interfaces* **2016**, *8*, 9829.

[27] J. Veres, S. D. Ogier, S. W. Leeming, D. C. Cupertino, S. Mohialdin Khaffaf, *Adv. Funct. Mater.* **2003**, *13*, 199.

[28] Y. Krupskaya, M. Gibertini, N. Marzari, A. F. Morpurgo, *Adv. Mater.* **2015**, *27*, 2453.

[29] I. Yu. Chernyshov, M. V. Vener, E. V. Feldman, D. Yu. Paraschuk, A. Yu. Sosorev, *J. Phys. Chem. Lett.* **2017**, *8*, 2875.

[30] U. Sondermann, A. Kutoglu, H. Bassler, *J. Phys. Chem.* **1985**, *89*, 1735.

[31] R. W. I. de Boer, M. Jochemsen, T. M. Klapwijk, A. F. Morpurgo, J. Niemax, A. K. Tripathi, J. Pflaum, *J. Appl. Phys.* **2004**, *95*, 1196.

[32] M. A. Lampert, A. Rose, R. W. Smith, *J. Phys. Chem. Solids* **1959**, *8*, 464.

[33] V. Podzorov, S. E. Sysoev, E. Loginova, V. M. Pudalov, M. E. Gershenson, *Appl. Phys. Lett.* **2003**, *83*, 3504.

[34] O. D. Jurchescu, J. Baas, T. T. M. Palstra, *Appl. Phys. Lett.* **2004**, *84*, 3061.

[35] B. Fraboni, C. Femoni, I. Mencarelli, L. Setti, R. D. Pietro, A. Cavallini, A. Fraleoni-Morgera, *Adv. Mater.* **2009**, *21*, 1835.

[36] S. Fratini, S. Ciuchi, D. Mayou, G. T. de Laissardière, A. Troisi, *Nat. Mater.* **2017**, *16*, 998.

[37] G. D'Avino, Y. Olivier, L. Muccioli, D. Beljonne, *J. Mater. Chem. C* **2016**, *4*, 3747.

[38] G. D'Avino, L. Muccioli, F. Castet, C. Poelking, D. Andrienko, Z. G. Soos, J. Cornil, D. Beljonne, *J. Phys. Condens. Matter* **2016**, *28*, 433002.

[39] T. F. Harrelson, V. Dantanarayana, X. Xie, C. Koshnick, D. Nai, R. Fair, S. A. Nuñez, A. K. Thomas, T. L. Murrey, M. A. Hickner, J. K. Grey, J. E. Anthony, E. D. Gomez, A. Troisi, R. Faller, A. J. Moulé, *Mater. Horiz.* **2019**, *6*, 182.

[40] G. Schweicher, G. D'Avino, M. T. Ruggiero, D. J. Harkin, K. Broch, D. Venkateshvaran, G. Liu, A. Richard, C. Ruzié, J. Armstrong, A. R. Kennedy, K. Shankland, K. Takimiya, Y. H. Geerts, J. A. Zeitler, S. Fratini, H. Sirringhaus, *Adv. Mater.* **2019**, *31*, 1902407.

[41] A generalized density of states (GDOS) is the phonon spectrum measured from inelastic neutron scattering. In contrast to the vibrational density of states (see ref. [42]), the GDOS involves a weighting of the scatterers (ions) with their scattering powers σ/M (σ: scattering cross section, M: mass).

[42] S. N. Taraskin, S. R. Elliott, *Phys. Rev. B* **1997**, *55*, 117.

[43] A. Girlando, L. Grisanti, M. Masino, I. Bilotti, A. Brillante, R. G. Della Valle, E. Venuti, *Phys. Rev. B* **2010**, *82*, 035208.

[44] R. S. Sánchez-Carrera, P. Paramonov, G. M. Day, V. Coropceanu, J.-L. Brédas, *J. Am. Chem. Soc.* **2010**, *132*, 14437.

[45] G. Schweicher, V. Lemaur, C. Niebel, C. Ruzié, Y. Diao, O. Goto, W.-Y. Lee, Y. Kim, J.-B. Arlin, J. Karpinska, A. R. Kennedy, S. R. Parkin, Y. Olivier, S. C. B. Mannsfeld, J. Cornil, Y. H. Geerts, Z. Bao, *Adv. Mater.* **2015**, *27*, 3066.

[46] R. Ozdemir, S. Park, I. Deneme, Y. Park, Y. Zorlu, H. A. Alidagi, K. Harmandar, C. Kim, H. Usta, *Org. Chem. Front.* **2018**, *5*, 2912.

[47] Y.-C. Chang, Y.-D. Chen, C.-H. Chen, Y.-S. Wen, J. T. Lin, H.-Y. Chen, M.-Y. Kuo, I. Chao, *J. Org. Chem.* **2008**, *73*, 4608.